PCCP

Dynamic Article Links ▶

www.rsc.org/pccp

PAPER

Thin silica films on Ru(0001): monolayer, bilayer and three-dimensional networks of [SiO₄] tetrahedra†

Bing Yang,[a] William E. Kaden,[a] Xin Yu,[a] Jorge Anibal Boscoboinik,[a]
Yulia Martynova,[a] Leonid Lichtenstein,[a] Markus Heyde,[a] Martin Sterrer,[a]
Radosław Włodarczyk,[b] Marek Sierka,*[bc] Joachim Sauer,[b] Shamil Shaikhutdinov*[a]
and Hans-Joachim Freund[a]

The atomic structure of thin silica films grown over a Ru(0001) substrate was studied by X-ray photoelectron spectroscopy, infrared reflection absorption spectroscopy, low energy electron diffraction, helium ion scattering spectroscopy, CO temperature programmed desorption, and scanning tunneling microscopy in combination with density functional theory calculations. The films were prepared by Si vapor deposition and subsequent oxidation at high temperatures. The silica film first grows as a monolayer of corner-sharing [SiO₄] tetrahedra strongly bonded to the Ru(0001) surface through the Si–O–Ru linkages. At increasing amounts of Si, the film forms a bilayer of corner-sharing [SiO₄] tetrahedra which is weakly bonded to Ru(0001). The bilayer film can be grown in either the crystalline or vitreous state, or both coexisting. Further increasing the film thickness leads to the formation of vitreous silica exhibiting a three-dimensional network of [SiO₄]. The principal structure of the films can be monitored by infrared spectroscopy, as each structure shows a characteristic vibrational band, *i.e.*, ~1135 cm⁻¹ for a monolayer film, ~1300 cm⁻¹ for the bilayer structures, and ~1250 cm⁻¹ for the bulk-like vitreous silica.

Introduction

Silicon dioxide (SiO₂) is one of the key materials in many modern technological applications ranging from integrated circuits to supports for catalysts. In the last decade, thin silica films grown on metal substrates have been used as model systems well-suited for studying structure–property relationships of silica-based materials, since the geometric, electronic and chemical properties of the silica films can be examined on the atomic scale by employing a variety of surface sensitive techniques as well as computational methods.[1–11] In particular, it has been shown that crystalline silica films grown on Mo(112) consist of a single layer of corner sharing [SiO₄] tetrahedra thus forming a honeycomb-like network with a SiO₂.₅ composition (the so-called "monolayer" silica film, Fig. 1a).[9–11] Thicker silica films on Mo(112), as well as other Mo substrates, exhibited a non-crystalline structure.[1–3,12] The preparation of crystalline silica films has been reported on Pd(100)[13] and Ni(111),[14] albeit the atomic structures of the films were not established.

Very recently, we have reported the preparation and the atomic structure of SiO₂ films grown on Ru(0001) where corner sharing [SiO₄] tetrahedra form a bilayer (Fig. 1b), which is structurally similar to layered sheet silicate minerals (diphyllosilicates).[15] In addition, reversible adsorption of the oxygen atoms directly on the metal surface underneath the silica film was observed, resulting in the so-called "O-rich" or "O-poor" films.[16] In contrast to the Mo(112) support, the bilayer film is bound to Ru(0001) primarily through the weak van der Waals interaction. This considerably reduces the extent to which the metal support may influence the reactivity of the silica films towards ambient gases and deposited clusters, thus rendering the bilayer film a more suitable model system.

In this work, we examine the growth of silica films on Ru(0001) in more detail. In particular, we focus on the dependence of the atomic structure of the film on variations in overlayer thickness and film growth conditions. For this, we make use of X-ray photoelectron spectroscopy (XPS), infrared reflection absorption spectroscopy (IRAS), low energy electron diffraction (LEED), helium ion scattering spectroscopy (ISS),

ᵃ Abteilung Chemische Physik, Fritz-Haber-Institut der Max-Planck-Gesellschaft, Faradayweg 4-6, 14195 Berlin, Germany. E-mail: shaikhutdinov@fhi-berlin.mpg.de
ᵇ Institut für Chemie, Humboldt-Universität zu Berlin, Brook-Taylor-Straße 2, 12489 Berlin, Germany. E-mail: marek.sierka@chemie.hu-berlin.de
ᶜ Institut für Materialwissenschaft und Werkstofftechnologie, Friedrich-Schiller-Universität Jena, Löbdergraben 32, 07743 Jena, Germany
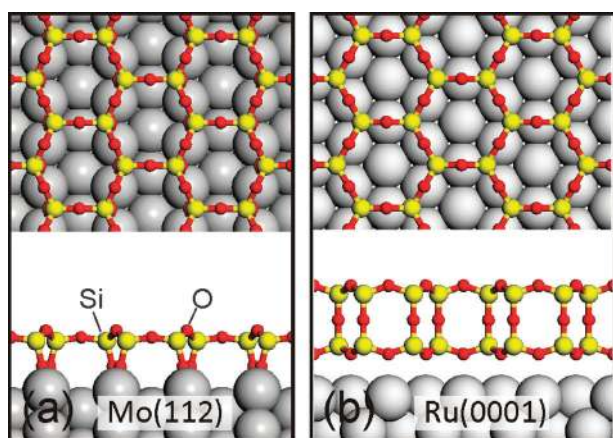
Fig. 1 Top and cross-sectional views of (a) $SiO_{2.5}/Mo(112)$[10] and (b) $SiO_2/Ru(0001)$[15] films.

CO temperature programmed desorption (TPD) and scanning tunneling microscopy (STM) in combination with density functional theory (DFT) calculations. The results reveal a structural complexity of the silica overlayers and provide further steps towards our understanding of the structure and reactivity of the silica-based systems.

Experimental and computational methods

The experiments were carried out within two separate ultrahigh vacuum (UHV) chambers. The first chamber (base pressure $\sim 5 \times 10^{-10}$ mbar) is equipped with low-energy electron diffraction (LEED, from Omicron), XPS with a Scienta SES 200 hemispherical analyzer, IRAS (Bruker IFS 66v), and STM (Omicron), while the second (base pressure $\sim 1.5 \times 10^{-10}$ mbar) is equipped with a mass spectrometer (Pfeiffer), LEED (Specs), and a hemispherical analyzer (Specs) that is used for both ISS and XPS measurements. In both cases, the Ru(0001) crystal (from MaTeck) was mounted on an Omicron sample holder, and the temperature was measured by a K-type thermocouple spot-welded to the edge of the crystal. A pyrometer has been employed as an internal reference to ensure self-consistency at higher sample temperatures.

The clean Ru(0001) surface was obtained by repeated cycles of Ar^+-sputtering and annealing to 1300 K under UHV. The $3O(2 \times 2)$–Ru(0001) surface was prepared by exposing the clean surface to 3×10^{-6} mbar O_2 at 1200 K for 5 min and then cooling to 500 K prior to evacuating the oxygen from the chamber. Silicon (99.99%) was deposited onto the $3O(2 \times 2)$–Ru(0001) surface in 2×10^{-7} mbar O_2 using an e-beam assisted evaporator (EMT3, Omicron). During evaporation the substrate was biased at the same potential as the Si rod to prevent acceleration of ions toward the sample, which could create uncontrolled defects. Final oxidation was performed in 3×10^{-6} mbar O_2 at ~ 1200 K. The amount of Si at the surface was measured by XPS using the well-established structure of $SiO_{2.5}/Mo(112)$ as a reference.[10,11] For direct comparison, we provide XPS spectra and thickness dependent quantitative trends in Fig. S1 of the ESI.† The XP-spectra were referenced by setting the Au $4f_{7/2}$ level to 84.0 eV measured on a clean gold foil. The IRA-spectra were recorded using p-polarized light at 84° grazing angle of incidence (resolution 4 cm^{-1}).

CO TPD spectra were collected with a differentially pumped mass spectrometer following 5 L (1 L $= 10^{-6}$ Torr s) exposures to ^{13}CO at ~ 180 K using a heating rate of 3 K s^{-1}. He$^+$ ISS measurements were made using a nominal beam energy, scattering angle, and surface flux of 1 keV, 135°, and ~ 100 nA, respectively. STM images were acquired at room temperature using Pt–Ir tips.

All calculations are based on density functional theory (DFT) and were carried out using Vienna *ab initio* simulation package (VASP),[17,18] along with the Perdew–Burke–Ernzerhof (PBE)[19,20] exchange–correlation functional. The electron–ion interactions were described by the projector augmented wave (PAW) method, originally developed by Blöchl[21] and adapted by Kresse and Joubert.[22] Only the valence electrons were explicitly considered. An empirical dispersion correction was added to qualitatively account for the dispersion forces (PBE + D).[23,24] Unless stated otherwise, a 400 eV cutoff for the plane wave basis set and an $8 \times 4 \times 1$ Monkhorst–Pack grid[25] for the integrations of the first Brillouin zone were used. The positions of nuclei were relaxed until the forces were smaller than 10^{-3} eV Å^{-1}. Harmonic vibrational frequencies were calculated using a central finite difference method with 0.02 Å displacements of the atoms in each Cartesian direction. The intensities were obtained from the derivatives of the dipole moment component perpendicular to the surface. To compensate for systematic errors of DFT, the vibrational frequencies are scaled by an empirical factor of 1.0341 derived from a comparison between experimental[26,27] and calculated frequencies for α-quartz (see supplemental material in ref. 15). The core-level energies were calculated including final state effects using a modified PAW method.[28]

The Ru(0001) substrate was constructed from relaxed bulk hexagonal close packed structure with calculated lattice constants of $a = 2.698$ Å and $c = 4.243$ Å, in excellent agreement with the experimental values of $a = 2.696$ Å and $c = 4.269$ Å.[29] Bulk structure optimization has been carried out using a 1200 eV cutoff for the plane wave basis set and a $13 \times 13 \times 8$ Monkhorst–Pack grid[25] for the integrations of the first Brillouin zone. The surface slabs were modeled using an orthorhombic 2×2 supercell, with $a_0 = 5.396$ Å and $b_0 = 9.346$ Å, containing five Ru layers, with three top layers allowed to relax and two bottom layers fixed to their bulk positions.

The stability of different $Si_mO_n/Ru(0001)$ surface models is compared using Gibbs energies of formation per surface area A, $\Delta\gamma$

$$\Delta\gamma = \frac{1}{A}\left[\Delta E_{form} - m\Delta\mu_{Si} - \frac{n}{2}\Delta\mu_{O_2}\right], \qquad (1)$$

where ΔE_{form} is the surface formation energy according to the reaction

$$Ru(0001) + mSi_{bulk} + \frac{n}{2}O_2 \rightarrow Si_mO_n/Ru(0001), \qquad (2)$$
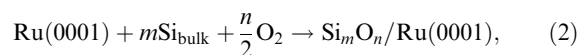
and $\Delta\mu_{Si}$ as well as $\Delta\mu_{O_2}$ are relative silicon and oxygen chemical potentials. They are defined as $\Delta\mu_{Si} = \mu_{Si} - E_{Si_{bulk}}$ and $\Delta\mu_{O_2} = \mu_{O_2} - E_{O_2}$, with μ_{Si} and μ_{O_2} as silicon and oxygen chemical potentials, and $E_{Si_{bulk}}$ and E_{O_2} as the bulk Si and molecular O_2 energies, respectively. The relative chemical potentials $\Delta\mu_X$ can be related to experimental conditions using standard thermodynamics.

Results and discussion

In the previously reported preparation of the bilayer silica film[15] Si was vapor-deposited onto the oxygen precovered O(2×1)–Ru(0001) surface at elevated temperatures ($\sim$630 K) in ambient oxygen (typically 10^{-7} mbar). The presence of chemisorbed oxygen presumably prevents intermixing of Si and Ru, and supplies more reactive, *i.e.* atomic, oxygen species for oxidation of the Si deposits than molecular oxygen in the gas phase. Indeed, it was found by XPS that the O ad-atoms were all consumed upon Si deposition. However, under the conditions studied, silicon was not fully oxidized. The complete oxidation, accompanied by film ordering, only occurred upon subsequent high temperature annealing in oxygen.

Analysis of the experimental results, obtained in attempts to find the best recipe for growing the bilayer silica film on Ru(0001), led us to some modifications to the previously reported preparation. First, we used the $3O(2 \times 2)$–Ru(0001) surface (instead of O(2×1)–Ru(0001)), because (i) it exhibits the highest coverage of *chemisorbed* oxygen that could be formed under UHV;[30] and (ii) it shares the same arrangement of the oxygen atoms as the topmost O-layer in the bilayer silica film, and as such may have a template effect. Second, we lowered the substrate temperature during the Si deposition to $\sim$100 K. This alteration stemmed from our previous studies of the growth of CeO$_2$(111) films on the same Ru(0001) support, where deposition at low temperatures considerably improved the film adhesion despite a very large lattice mismatch ($\sim$40%).[31] It seems to be plausible that lower temperatures suppress the diffusivity of atoms on the surface, thereby favoring the formation of two-dimensional structures prior to final oxidation at high temperatures.

Therefore, in the following film preparations we vary only the amounts of Si deposited while keeping other parameters fixed, if not specified, *i.e.* Si was deposited onto the $3O(2 \times 2)$–Ru(0001) surface at $\sim$100 K in 2×10^{-7} mbar O$_2$ and then annealed at $\sim$1200 K for 5 min in 3×10^{-6} mbar O$_2$. For simplicity, the Si coverage is presented in the text in monolayer equivalent (MLE) such that 2 MLE corresponds to the amount of Si necessary to grow a bilayer film.

Monolayer silica films

Under the assumption that silica films on Ru(0001) grow exclusively as a bilayer, deposition of 1 MLE Si would result in the film covering only $\sim$50% of the Ru(0001) surface. However, a large scale STM image of such a film (Fig. 2a) shows that the surface becomes almost fully covered by the silica film with small pits and holes decorated by nanoparticles. The flat terraces expose multiple domains, all showing a honeycomb-like structure with a 5.4 Å periodicity (Fig. 2b). The periodicity agrees with the (2×2)-Ru(0001) diffraction pattern observed by LEED (not shown). The domains are shifted by a half of the lattice with respect to each other, thus producing a network of anti-phase domain boundaries imaged as protruding lines. The randomly distributed holes are $\sim$1.4 Å in apparent depth, as shown in Fig. 2(c) and (d). Certainly, this value is much smaller than the "geometrical" thickness of the bilayer film, of the order of 5 Å (Fig. 1b).

Indeed, the IRA-spectrum (Fig. 3a) does not show any band around 1300 cm^{-1}, which is a benchmark for the Si–O–Si
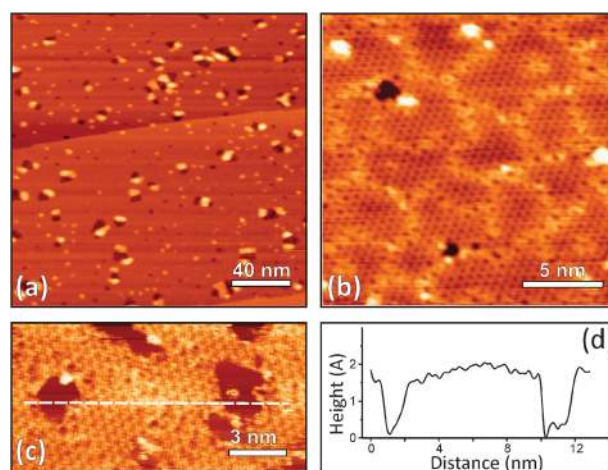

Fig. 2 STM images of the 1 MLE silica film on Ru(0001). The 2 Å-high step running across the image (a) is assigned to the monoatomic step of Ru(0001) underneath the film. The profile line in (d) is measured along the line indicated in (c). (Tunneling parameters: $U = 8$ V; $I = 0.1$ nA (a); 2.0 V, 0.1 nA (b); 1.2 V, 0.1 nA (c).)

linkage normal to the surface in the bilayer film (Fig. 1b). Instead, a sharp signal at 1134 cm^{-1} dominates the spectrum, which also shows peaks at 1074, 790 and 687 cm^{-1}. (Note, that the $3O(2 \times 2)$–Ru(0001) surface is IR-silent in the region above 600 cm^{-1}.) In fact, this spectrum resembles spectra reported for SiO$_{2.5}$/Mo(112) films, with a sharp and intense band at 1060 cm^{-1}, assigned to the stretching vibrations of the Si–O–Mo linkage, and weak signals at 770 and 675 cm^{-1}.[10]

XPS inspection of this film showed only one state in the Si2p region with a binding energy (BE) of 102.3 eV, which is characteristic of Si^{4+}. The spectrum for the O1s core level (Fig. 3b) showed, at least, two components centered at 531.3 and 529.8 eV, with a peak area ratio of roughly 3:2. It should be mentioned, however, that precise deconvolution may be affected by the presence of the silica nanoparticles seen in Fig. 2a. Note also that the position of the low energy peak (529.8 eV) is close to that observed on the $3O(2 \times 2)$–Ru(0001) surface prior to the Si deposition and as such can partly be attributed to the small holes exposing the O/Ru surface (see Fig. 2). Nonetheless, the peak separation and the intensity ratio are similar to those found for the SiO$_{2.5}$/Mo(112) films (1.3 eV and 3:2, respectively),[11] where the high BE signal is associated with the oxygen atoms forming the Si–O–Si bonds, and the low BE signal corresponds to interfacial O species having bonds to the Mo substrate, *i.e.* to the Si–O–Mo linkages.
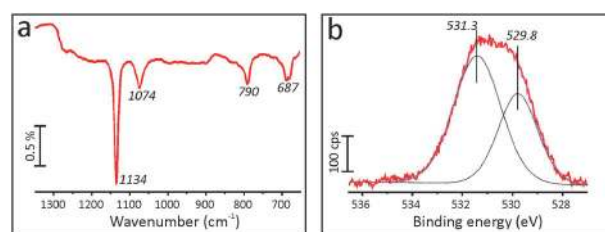

Fig. 3 IRA-spectrum (a) and XP-spectrum of the O1s core level (b) of the 1 MLE film (see the STM image in Fig. 2). XP-spectrum is deconvoluted into two peaks as indicated.

11346 | *Phys. Chem. Chem. Phys.*, 2012, **14**, 11344–11351

This journal is © the Owner Societies 2012

Given the STM results, showing the formation of a complete overlayer with (2 × 2) lattice structure, and the strong agreement between XPS and IRAS results for this film with those previously reported for SiO$_{2.5}$/Mo(112),[10,11] we suggest a similar growth-mode for silica films over Ru(0001) under our conditions (below 1 MLE). Namely, we suggest a honeycomb shaped network of tetrahedral Si–O linkages with a 5.4 Å lattice constant, in which every Si makes one Si–O–Ru bond and three bridging Si–O–Si bonds. This conclusion is in agreement with depth-dependent ISS results (see Fig. S2 in the ESI†), which show Si saturation at 1 MLE (i.e. the film forms a complete overlayer at this coverage).

Bilayer silica films

In the next step, we deposited another 1 MLE Si on top of the prepared monolayer silica film at 100 K, and again oxidized in 3×10^{-6} mbar O$_2$ at 1200 K for 5 min. The IRAS measurements immediately showed an intense band at 1300 cm^{-1} with concomitant disappearance of the 1134 cm^{-1} band, indicating the formation of the bilayer film at the expense of the monolayer structure (Fig. 4a). Obviously, such transformation must be accompanied by breaking Si–O–Ru bonds while creating the Si–O–Si linkages, which is a thermodynamically unfavorable process in the case of the Mo(112) support, where the formation of bilayer films has never been observed. Therefore, under our conditions, it is the Si coverage that governs the structure of the silica films on Ru(0001). Indeed, experiments with an intermediate coverage of ∼1.5 MLE Si deposited in one step reveal the coexistence of mono- and bilayer structures, where both the 1300 and 1134 cm^{-1} bands are detected (Fig. 4c). STM images of the resulting films revealed flat morphology where wide terraces of Ru(0001) can still be recognized (Fig. 4d). Large domains within the same terrace are separated by steps with apparent heights of ∼1.5 and ∼5 Å when measured with respect to small holes exposing the underlying O–Ru surface. The 1.5 Å-high steps can straightforwardly be assigned to the monolayer structures, thus indicating an apparent thickness of ∼5 Å for the bilayer films, i.e. in good agreement with the model presented in Fig. 1b.

Depending on the preparation conditions, LEED patterns of the bilayer films may show both (2 × 2) spots and a diffraction ring (see, for example, the LEED inset in Fig. 4a). The latter indicates the presence of randomly oriented rotational domains like in powders. Indeed, the respective STM images revealed domains of ordered structures (marked by a circle in Fig. 4b) coexisting with disordered structures, which could be identified as two-dimensional, vitreous silica.[32,33] Analysis of bilayer films prepared under different conditions by varying annealing time, temperature, oxygen pressure, etc. showed that the rate of sample cooling after the high-temperature oxidation step plays an important role in controlling film crystallinity.

To illustrate this effect, Fig. 5 shows the LEED and STM results for two samples, both possessing the same amount of Si (∼2 MLE) deposited at 100 K. The sample prepared by slow cooling (below 1 K s^{-1}) shows a sharp (2 × 2) LEED pattern and a regular honeycomb-like structure in STM, whereas the sample prepared by relatively fast cooling (∼5 K s^{-1}) shows a diffraction ring in addition to the (2 × 2) pattern. Although the atomic structure could not be resolved in these images, the
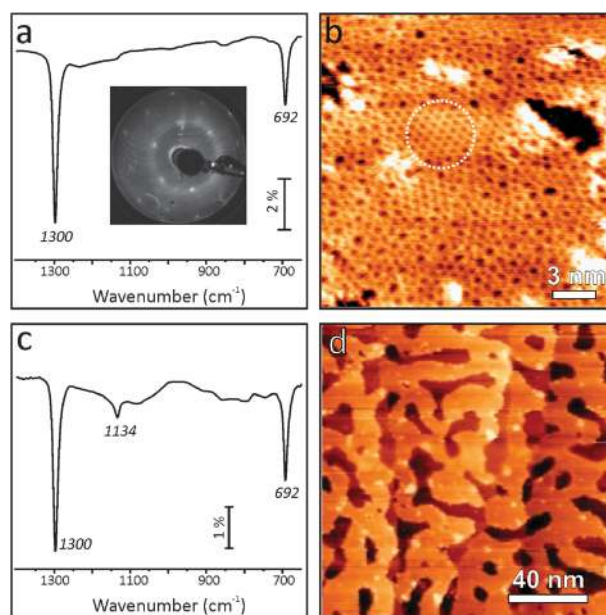

Fig. 4 (a) and (b) IRA-spectrum and a high-resolution STM image of the 2 MLE silica film prepared by two sequential deposition and oxidation steps of 1 MLE Si each. The respective LEED pattern (at 60 eV) is shown as an inset in (a). The dashed circle in (b) marks the ordered silica surface. IRA-spectrum (c) and a large-scale STM image (d) of the 1.5 MLE silica film deposited in one step. Both the bilayer and the monolayer structures are formed, with the characteristic phonons at 1300 and 692 cm^{-1} (bilayer) and 1134 cm^{-1} (monolayer). (Tunneling parameters applied for STM images: 2 V, 0.1 nA (b); 8.0 V, 0.1 nA (d).)

vitreous state of the silica film is easily recognized.[33] Atomic size depressions in the respective STM images (Fig. 4b and 5) correspond to the "pores" formed by a random network of corner sharing [SiO$_4$] tetrahedra. In the crystalline phase, the
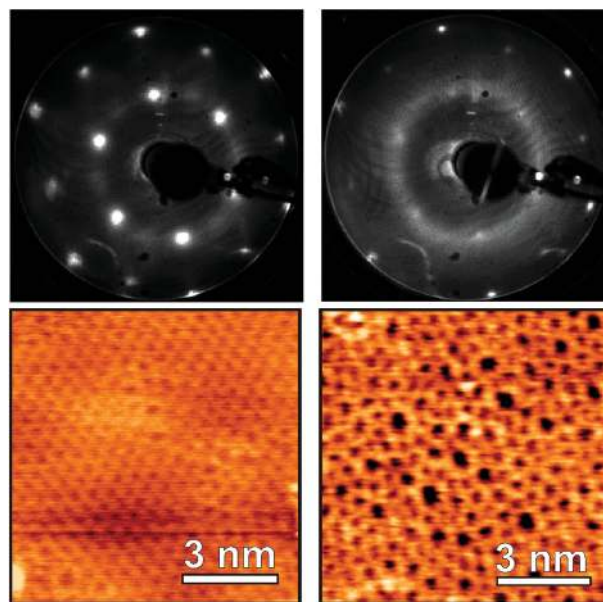

Fig. 5 (top) LEED patterns (at 60 eV) and STM images (bottom) of the bilayer silica films prepared by slow (on the left) and fast (on the right) cooling after the high temperature oxidation step in the film preparation. (Tunneling parameters: 2 V, 0.1 nA (left); 3.3 V, 0.1 nA (right).)

regular honeycomb-like structure is formed by six [SiO₄] units (see Fig. 1). By contrast, the number varies between 4 and 9 for the vitreous silica film, which ultimately leads to pores (depressions) of different sizes. Interestingly, XPS and IRAS measurements do not detect substantial differences between the crystalline and vitreous films. Note also that once formed, the vitreous film, prepared by fast cooling, cannot be transformed into the crystalline state by re-oxidation of the same sample followed by slow cooling, and *vice versa*. Applying higher temperatures leads to the film decomposition. We have also examined the influence of the cooling rate on the structure of the monolayer silica films. Basically, no effect was observed. Most likely the strong Si–O–Ru bonds drive the monolayer film to be in registry with a Ru(0001) substrate, thus resulting in well-ordered monolayer films as shown in Fig. 2.

To further investigate the differences between crystalline and vitreous bilayer films, we provide Fig. 6, which shows results from He$^+$ ISS and CO TPD measurements for two samples prepared in the same manner as those in Fig. 5, as well as the equivalent data collected after making those films "O-poor" *via* heating to 1180 K for 20 min. The first thing to note when looking at the ISS spectra is that the vitreous and crystalline samples yield nearly identical peak intensities for all elements detected despite having clearly different degrees of ordering. Since ISS is predominantly sensitive to only those atoms in the top-most layer of the sample,[34] this finding suggests that both films posses roughly equivalent terminal stoichiometries, *i.e.* in agreement with our previously reported STM findings.[33] We estimate an O : Si termination stoichiometry of ∼3 : 2 when using the well known (7 × 7) reconstruction of Si(111) and known coverages of oxygen chemisorbed on Ru(0001) to calibrate relative sensitivities of these two peaks. Again, this value is in good agreement with structural models of the bilayer films.

In contrast with the ISS results, we do note clear differences between the vitreous and crystalline films when probing with CO TPD, but only after depleting the samples of sub-silica, only Ru-bound, oxygen (Fig. 6b). Before heating the films to desorb these oxygen atoms, however, we observe TPD spectra that are nearly identical to each other and those detected from uncovered 3O(2 × 2)–Ru(0001). However, the total amount of CO is only on the order of ∼1%, which suggests defect mediated adsorption on these surfaces. In the case of the crystalline film, we note little, if any, variation in the TPD spectrum after inducing the "O-poor" state. In contrast,
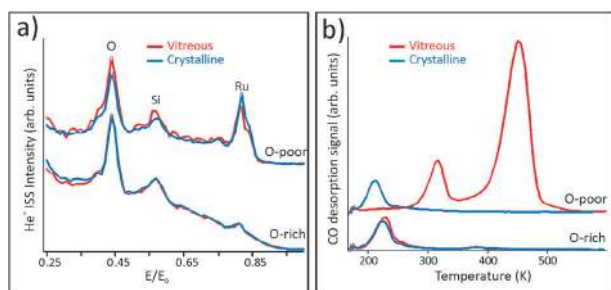
CO TPD taken from "O-poor" vitreous films show starkly different behavior. Both the peak temperatures and intensities increase significantly, such that ∼10× more CO now desorbs from the sample in a bimodal fashion, with peaks centered at ∼320 and 450 K. Similar TPD spectra, albeit with ∼20× more intensity, are observed for 3O(2 × 2)–Ru(0001) samples after undergoing the same "O-poor" treatment, which causes a transition to the O(2 × 2) phase according to the peak positions.[35] Compared with the results for crystalline films, this finding allows us to ascribe the additional desorption features to binding sites within less confined areas of the vitreous film (*i.e.* open patches or larger ring structures), and we estimate that the concentration of these sites should be ∼5% of the total film. The latter value is consistent with the concentration of larger-than 7-member silica rings previously noted by STM in the vitreous films.[33] Therefore, it is believed that the majority of additional binding sites allotted to CO over the vitreous silica come from the presence of these larger rings, in addition to any increase in the abundance of defective "holes" in the film.

To better understand the factors controlling the formation of one film relative to the other, we have independently varied several of the parameters thought to influence the film growth. In particular, we found that lower deposition temperatures appear to favor the formation of more crystalline films. This likely implies the formation of more two-dimensional SiO$_x$ overlayers at lower temperatures, which may form as a result of more limited surface diffusivity. When such films are then oxidized at high temperatures, the increased wetting of the precursor state is then presumably reflected in the final state of the prepared film. This scenario is supported by the fact that Si deposited at ∼100 K ultimately leads to the formation of more dense films than those deposited at, for example, 300 K, as evidenced by comparative STM and CO IRAS studies (not shown). Therefore, it appears that not only the kinetics (*via* the cooling rate) but also the precursor state (two-dimensional *vs.* three-dimensional) governs the silica film ordering. Interestingly, bilayer films created *via* metal evaporation at room temperature were better crystallized upon deposition of a bit more than 2 MLE Si, regardless of the cooling rate. All in all, the bilayer film ordering seems to depend on many parameters and their particular combination.

"Thick" silica films

To see whether the bilayer silica film can be further grown in a layer-by-layer manner, we have examined films prepared by deposition of 4 MLE Si. The results were to a minor extent dependent on whether the films were prepared in one step or in two sequential 2 MLE deposition–oxidation steps. Based on the XPS results, slightly higher temperatures (by 25 K) were necessary to fully oxidize the films.

Fig. 7 shows a large-scale STM image of the 4 MLE film, which reveals the smooth surface, albeit not atomically flat. No additional features were observed in LEED (see the inset in Fig. 7) beyond the (2 × 2) diffraction spots and the ring. Unfortunately, attempts to achieve atomic resolution were not successful, as our STM became unstable at lower biases since tunneling probability strongly attenuates for the
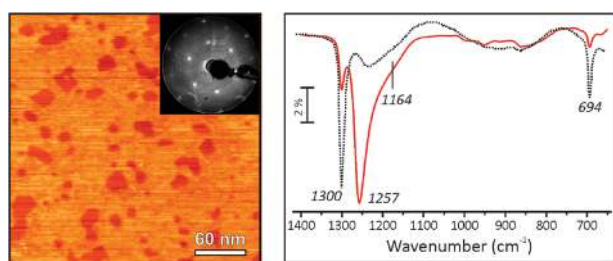

Fig. 6 (a) He$^+$ ISS of O-rich and O-poor 2 MLE silica films with varying degrees of crystallinity. (b) ^{13}CO TPD taken from the same films used in (a) (heating rate 3 K s^{-1}).

Fig. 7 STM image (on the left) and IRA-spectrum (on the right) of the 4 MLE film. The LEED pattern is shown in the inset. The dashed line shows the IRA-spectrum for the 2.2 MLE film, for comparison. (Tunneling parameters: 9 V, 0.1 nA.)

thick insulating films. However, we found that the depressed areas in this image exhibited the vitreous bilayer-like film with a characteristic "pore" structure (as shown in Fig. 5). With respect to these patches the rest areas are 6–8 Å higher, which would, in principle, be consistent with the growth of the second bilayer stack.

However, as in the case of mono- and bilayer structures, the substantial changes are observed in IRA-spectra. As shown in Fig. 7, a new band develops at 1257 cm^{-1} with a prominent shoulder at 1164 cm^{-1}, while the 1300 and 694 cm^{-1} peaks attenuate by a factor of three. The attenuation is, in principle, consistent with the fraction of the surface area covered by the bilayer structure, *i.e.* approximately 1/3. Although the intensity–coverage relationships in IRAS are not always straightforward, this finding suggests the coexistence of the bilayer and another silica structure, both adsorbed on Ru, rather than the growth of new form of silica on top of the bilayer film.

The band centered at 1257 cm^{-1} is virtually identical to that previously observed on several nanometers thick silica films grown on Mo(112),[4,7,12,36] Mo(110),[2,3] and Si(100).[37–39] In a similar way, bearing in mind the so-called Berreman effect[40] and the metal selection rules applied to IRAS,[41] the IRAS bands at 1257 and 1164 cm^{-1} can be assigned to the asymmetric longitudinal-optical vibration modes as in quartz-like compounds. It therefore appears that 4 MLE films exhibit a three-dimensional network of [SiO$_4$] tetrahedra rather than the layered structure observed for mono- and bi-layer films. In this case, the film may be differently terminated, resulting in relatively high surface corrugation as measured by STM (*ca.* 1 Å). Certainly, further experiments remain to be done to elucidate the surface structures of such "thick" vitreous films.

Computational results

When searching for the most stable silica structures under the experimental conditions investigated, we considered models of mono- and bi-layer silica films containing different numbers of oxygen O atoms adsorbed directly on the Ru(0001) surface (*i.e.* O(Ru) for clarity). In addition, the following ordered O–Ru(0001) structures[16] containing 2, 4, 6 and 8 O atoms per (2 × 2) unit cell, respectively, were used as models for oxygen-covered Ru(0001) substrates: O(2 × 2),[42] O(2 × 1),[43] 3O(2 × 2),[30] and O(1 × 1).[44] Models of the bilayer film, Si$_8$O$_{16}$·nO/Ru(0001), with n = 0, 2, 4, 6, and 8 O(Ru) atoms per unit cell were taken from our previous studies.[15,16] For the monolayer films,
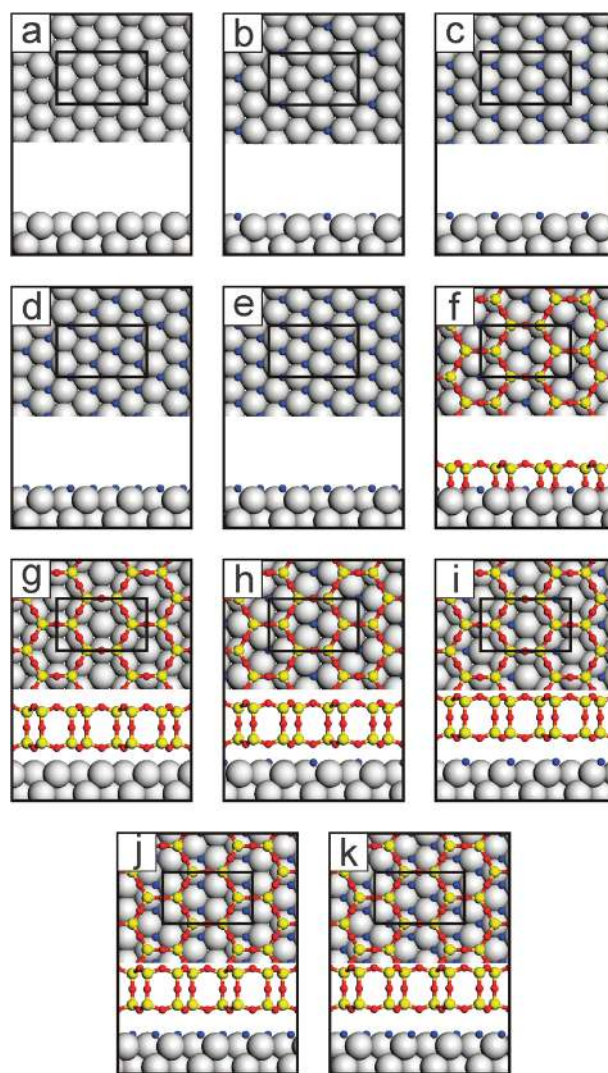

Fig. 8 Atomic structures of surface models: (a) Ru(0001), (b) O(2 × 2)–Ru(0001), (c) O(2 × 1)–Ru(0001), (d) 3O(2 × 2)–Ru(0001), (e) O(1 × 1)–Ru(0001), (f) Si$_4$O$_{10}$·2O/Ru(0001), (g) Si$_8$O$_{16}$/Ru(0001), (h) Si$_8$O$_{16}$·2O/Ru(0001), (i) Si$_8$O$_{16}$·4O/Ru(0001), (j) Si$_8$O$_{16}$·6O/Ru(0001), (k) Si$_8$O$_{16}$·8O/Ru(0001). Rectangles indicate (2 × 2) surface unit cells; Si yellow, O red and blue (when bonded to Ru only), Ru gray.

Si$_4$O$_{10}$·nO/Ru(0001), with n = 0–5, we adopted the structure of the silica monolayer on Mo(112).[10] These structures are shown in Fig. 8.

Fig. 9 displays a two-dimensional phase diagram, which shows the stability regions of the different phases computed as a function of $\Delta\mu_{O_2}$ (*i.e.* oxygen partial pressure) and $\Delta\mu_{Si}$ (*i.e.* amount of Si on the surface). At high values of $\Delta\mu_{Si}$ (*i.e.* ~0 eV) the silica bilayer is the most stable phase in the entire range of $\Delta\mu_{O_2}$. In the excess of oxygen (*i.e.* higher values of $\Delta\mu_{O_2}$) the oxygen atoms are adsorbed as O(Ru) on the metal surface underneath the silica film. This occurs at approximately the same values of $\Delta\mu_{O_2}$ as for clean Ru(0001), which is consistent with experimental findings that the desorption of the interfacial oxygen is observed in the same range of temperatures as the onset of the oxygen desorption on Ru(0001).[16] At very low values of $\Delta\mu_{Si}$ (~−6 eV) different oxygen-covered Ru(0001) structures are the most stable phases.
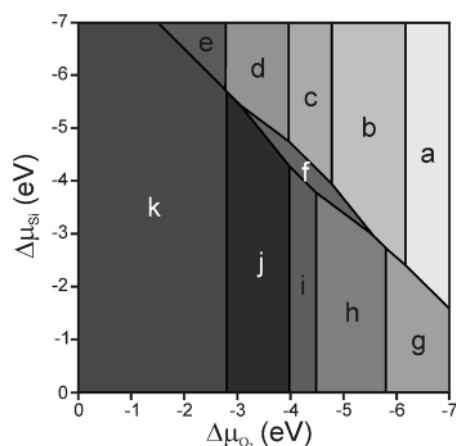
Fig. 9 Calculated phase diagram of 2D crystalline silica on a Ru(0001) substrate as a function of relative chemical potentials $\Delta\mu_{Si}$ and $\Delta\mu_{O_2}$. Letters denote regions of stability for the different phases depicted in Fig. 8.

The monolayer silica film is stable in a narrow region of chemical potentials. Among all of the monolayer models studied here ($n = 0$–5), only one, containing two O(Ru) atoms per unit cell (see Fig. 8f), was found to be stable. Fig. 10a shows the harmonic IRA spectrum simulated for this model, $Si_4O_{10}\cdot 2O/Ru(0001)$. Four IRA active modes are observed above 600 cm^{-1}. The most intensive mode at about 1160 cm^{-1} originates from the in-phase combination of asymmetric stretching vibrations of the Si–O–Ru linkages. The mode at 1076 cm^{-1} with very weak intensity involves combinations of symmetric O–Si–O stretching vibrations. Modes at 820 and 677 cm^{-1} are the combinations of asymmetric stretching of Si–O–Ru linkages and O–Si–O bending modes. The positions and relative intensities of these calculated bands are in good agreement with the experimental data provided in Fig. 3.

Fig. 10b shows calculated binding energy shifts of the O1s core levels. The simulated XP spectrum displays two groups of signals. The signal at higher BEs originates from oxygen atoms forming Si–O–Si bridges, and the three signals at lower BEs arise from oxygen atoms bound to the metal substrate, i.e., O(Ru) and those of the Si–O–Ru linkages in the different (top and hollow) sites with respect to Ru(0001). Again, as in the case of IRAS, the peak locations show good agreement with the XPS data obtained from the monolayer film (Fig. 3b).
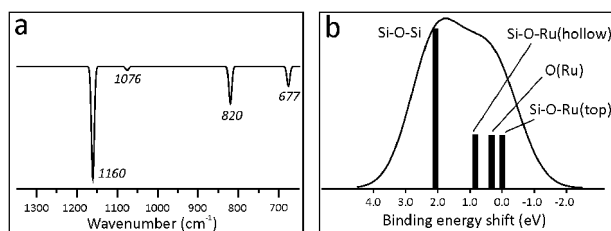
Conclusions

We have studied the growth and atomic structure of silica films prepared by Si deposition and high temperature oxidation on a Ru(0001) substrate using LEED, XPS, ISS, TPD, STM and IRAS. Silica first grows as a monolayer of corner-sharing [SiO$_4$] tetrahedra chemisorbed on Ru(0001), thus forming honeycomb-like structure very similar to the SiO$_{2.5}$ films previously reported on Mo(112). At increasing thickness the silica grows in the form of a bilayer or silicate-like SiO$_2$ sheet weakly bonded to Ru(0001). When depositing even more Si, we begin to form silica films, which exhibit a three-dimensional network rather than the layered structure observed for the thinner films. The principal structure of the film can be determined by infrared spectroscopy as each structure exhibits a characteristic vibrational band, i.e., $\sim$1135 cm^{-1} for the monolayer films, $\sim$1300 cm^{-1} for the bilayer sheet structures, and $\sim$1250 cm^{-1} for the bulk-like silica. Depending on the preparation conditions, the bilayer films can be prepared either in the crystalline or the vitreous state. The bilayer film ordering seems to be a delicate balance of many preparation parameters such as the Si deposition temperature, Si coverage and the rate of cooling after the high-temperature oxidation.

Finally, the results presented here indicate that the atomic structure of ultrathin silica films on metal supports is dependent on the nature of the support material (e.g. Mo(112) vs. Ru(0001)). This issue has been addressed explicitly in our very recent study,[45] which has shown that the metal–oxygen bond strength plays the decisive role in governing the atomic structure of the silica overlayers on metals. Metals with high oxygen adsorption energy favor the formation of the crystalline monolayer SiO$_{2.5}$ films, whereas noble metals form primarily vitreous SiO$_2$ bilayer films. Metals with intermediate energies, like Ru studied here, may form either of the structures or both coexisting.

Notes and references

1 J. W. He, X. Xu, J. S. Corneille and D. W. Goodman, Surf. Sci., 1992, 279, 119.
2 X. P. Xu and D. W. Goodman, Appl. Phys. Lett., 1992, 61, 774.
3 X. P. Xu and D. W. Goodman, Surf. Sci., 1993, 282, 323.
4 T. Schroeder, J. B. Giorgi, M. Baumer and H.-J. Freund, Phys. Rev. B: Condens. Matter Mater. Phys., 2002, 66, 11.
5 M. S. Chen, A. K. Santra and D. W. Goodman, Phys. Rev. B: Condens. Matter Mater. Phys., 2004, 69, 7.
6 M. S. Chen and D. W. Goodman, Surf. Sci., 2006, 600, L255.
7 T. K. Todorova, M. Sierka, J. Sauer, S. Kaya, J. Weissenrieder, J. L. Lu, H. J. Gao, S. Shaikhutdinov and H.-J. Freund, Phys. Rev. B: Condens. Matter Mater. Phys., 2006, 73, 165414.
8 J. Seifert, D. Blauth and H. Winter, Phys. Rev. Lett., 2009, 103, 4.
9 L. Giordano, D. Ricci, G. Pacchioni and P. Ugliengo, Surf. Sci., 2005, 584, 225.
10 J. Weissenrieder, S. Kaya, J. L. Lu, H. J. Gao, S. Shaikhutdinov, H.-J. Freund, M. Sierka, T. K. Todorova and J. Sauer, Phys. Rev. Lett., 2005, 95, 076103.
11 S. Kaya, M. Baron, D. Stacchiola, J. Weissenrieder, S. Shaikhutdinov, T. K. Todorova, M. Sierka, J. Sauer and H.-J. Freund, Surf. Sci., 2007, 601, 4849.
12 D. J. Stacchiola, M. Baron, S. Kaya, J. Weissenrieder, S. Shaikhutdinov and H.-J. Freund, Appl. Phys. Lett., 2008, 92, 3.
13 Z. Zhang, Z. Q. Jiang, Y. X. Yao, D. L. Tan, Q. Fu and X.-H. Bao, Thin Solid Films, 2008, 516, 3741.
14 M. Kundu and Y. Murata, Appl. Phys. Lett., 2002, 80, 1921.

Fig. 10 Caption IRA-spectrum (a) and XP-spectrum (b) simulated for the monolayer, $Si_4O_{10}\cdot 2O/Ru(0001)$ structure model (see Fig. 8f). The frequency in computed IRA-spectrum is scaled by a factor of 1.0341.[15] The bar height is proportional to the number of the respective O atoms in the structure. BE shifts are given with respect to the lowest O1s state.

15 D. Löffler, J. J. Uhlrich, M. Baron, B. Yang, X. Yu, L. Lichtenstein, L. Heinke, C. Buchner, M. Heyde, S. Shaikhutdinov, H.-J. Freund, R. Wlodarczyk, M. Sierka and J. Sauer, *Phys. Rev. Lett.*, 2010, **105**, 4.

16 R. Wlodarczyk, M. Sierka, J. Sauer, D. Löffler, J. J. Uhlrich, X. Yu, B. Yang, I. M. N. Groot, S. Shaikhutdinov and H.-J. Freund, *Phys. Rev. B: Condens. Matter Mater. Phys.*, 2012, **85**, 0854031.

17 G. Kresse and J. Furthmüller, *Comput. Mater. Sci.*, 1996, **6**, 15.

18 G. Kresse and J. Furthmüller, *Phys. Rev. B: Condens. Matter*, 1996, **54**, 11169.

19 J. P. Perdew, K. Burke and M. Ernzerhof, *Phys. Rev. Lett.*, 1996, **77**, 3865.

20 J. P. Perdew, K. Burke and M. Ernzerhof, *Phys. Rev. Lett.*, 1997, **78**, 1396.

21 P. E. Blöchl, *Phys. Rev. B: Condens. Matter*, 1994, **50**, 17953.

22 G. Kresse and D. Joubert, *Phys. Rev. B: Condens. Matter Mater. Phys.*, 1999, **59**, 1758.

23 S. Grimme, *J. Comput. Chem.*, 2006, **27**, 1787.

24 T. Kerber, M. Sierka and J. Sauer, *J. Comput. Chem.*, 2008, **29**, 2088.

25 H. J. Monkhorst and J. D. Pack, *Phys. Rev. B: Solid State*, 1976, **13**, 5188.

26 R. K. Sato and P. F. McMillan, *J. Phys. Chem.*, 1987, **91**, 3494.

27 J. F. Scott and S. P. S. Porto, *Phys. Rev.*, 1967, **161**, 903.

28 L. Köhler and G. Kresse, *Phys. Rev. B: Condens. Matter Mater. Phys.*, 2004, **70**, 165405.

29 A. V. Morozkin and Y. D. Seropegin, *J. Alloys Compd.*, 2004, **365**, 168.

30 K. L. Kostov, M. Gsell, P. Jakob, T. Moritz, W. Widdra and D. Menzel, *Surf. Sci.*, 1997, **394**, L138.

31 M. Baron, O. Bondarchuk, D. Stacchiola, S. Shaikhutdinov and H.-J. Freund, *J. Phys. Chem. C*, 2009, **113**, 6042.

32 W. H. Zachariasen, *J. Am. Chem. Soc.*, 1932, **54**, 3841.

33 L. Lichtenstein, C. Buchner, B. Yang, S. Shaikhutdinov, M. Heyde, M. Sierka, R. Wlodarczyk, J. Sauer and H.-J. Freund, *Angew. Chem., Int. Ed.*, 2012, **51**, 404.

34 *Principles and applications of ion scattering spectrometry: surface chemical and structural analysis*, ed. J. W. Rabalais, Wiley, New York, 2003.

35 F. M. Hoffmann and M. D. Weisel, *Surf. Sci.*, 1991, **253**, 59.

36 S. Wendt, E. Ozensoy, T. Wei, M. Frerichs, Y. Cai, M. S. Chen and D. W. Goodman, *Phys. Rev. B: Condens. Matter Mater. Phys.*, 2005, **72**, 9.

37 C. T. Kirk, *Phys. Rev. B: Condens. Matter*, 1988, **38**, 1255.

38 K. T. Queeney, M. K. Weldon, J. P. Chang, Y. J. Chabal, A. B. Gurevich, J. Sapjeta and R. L. Opila, *J. Appl. Phys.*, 2000, **87**, 1322.

39 K. T. Queeney, N. Herbots, J. M. Shaw, V. Atluri and Y. J. Chabal, *Appl. Phys. Lett.*, 2004, **84**, 493.

40 D. W. Berreman, *Phys. Rev.*, 1963, **130**, 2193.

41 P. Hollins, *Surf. Sci. Rep.*, 1992, **16**, 51.

42 M. Lindroos, H. Pfnür, G. Held and D. Menzel, *Surf. Sci.*, 1989, **222**, 451.

43 H. Pfnür, G. Held, M. Lindroos and D. Menzel, *Surf. Sci.*, 1989, **220**, 43.

44 C. Stampfl, S. Schwegmann, H. Over, M. Scheffler and G. Ertl, *Phys. Rev. Lett.*, 1996, **77**, 3371.

45 X. Yu, B. Yang, J. A. Boscoboinik, S. Shaikhutdinov and H.-J. Freund, *Appl. Phys. Lett.*, 2012, **100**, 151608.

This journal is © the Owner Societies 2012

Phys. Chem. Chem. Phys., 2012, **14**, 11344–11351 | 11351